Structural basis of iron piracy by a prominent human gut symbiont

Augustinas Silale*, Yung Li Soo, Hannah Mark, Arnaud Basle, Bert van den Berg*

Biosciences Institute, Newcastle University, Framlington Place, Newcastle upon Tyne, NE2 4HH, United Kingdom

*Correspondence to: augustinas.silale@newcastle.ac.uk
bert.van-den-berg@newcastle.ac.uk

Abstract

Iron is an essential element that can be growth-limiting in microbial communities, particularly those present within host organisms. To acquire iron, many bacteria secrete siderophores, secondary metabolites that chelate ferric iron. These iron chelates can be transported back into the cell via TonB-dependent transporters in the outer membrane, followed by intracellular liberation of the iron. *Salmonella* produces siderophores during gut infection. In response to iron starvation, the human gut symbiont *Bacteroides thetaiotaomicron* upregulates an iron piracy system, XusABC, which steals iron-bound siderophores from the invading *Salmonella*. Here, we investigated the molecular details of ferric enterobactin uptake by the XusAB complex. Our crystal and cryogenic electron microscopy structures explain how the XusB lipoprotein recognises iron-bound siderophores and passes them on to the XusA TonB-dependent transporter for translocation across the outer membrane. Moreover, our results suggest that XusABC and homologous systems can transport a variety of siderophores with different iron-chelating functional groups.

Introduction

Iron is essential for most organisms, including almost all bacteria. It is a protein cofactor required for enzymatic reactions and electron transport during various cellular processes. While iron is one of the most abundant transition metals on Earth, its bioavailability is limited due to the extremely low solubility (~10^{-18} M) of its predominant ferric (Fe^{3+}) form at physiological pH[1]. Many Gram-negative bacteria release siderophores, iron-chelating secondary metabolites, into the environment which, once bound to ferric iron, can be transported back into the cell via TonB-dependent transporters in the outer membrane (OM)[2]. A classic example is enterobactin, which is produced by Enterobacteriaceae and consists of three iron-chelating catecholate groups connected via amide linkers to a cyclic triserine lactone[3,4]. Ferric enterobactin (FeEnt) is taken up by the FepA transporter in *E. coli*[5,6], and iron is liberated from the FeEnt complex inside the cell[7,8]. Siderophore-mediated iron scavenging is important for pathogens during infection, when the host restricts iron availability to starve invading bacteria via nutritional immunity[9,10]. Additionally, secreted siderophores are not necessarily taken up by the same bacterium that produced them, resulting in complex iron availability-dependent interactions in microbial communities[11].

The gastrointestinal tract is home to a complex community of microorganisms that cooperate and compete for available nutrients both with the host and between themselves[12,13]. Depriving the gut microbiota of iron eventually results in irreversible structural changes in gut microbial communities[14,15]. Bacteroidetes, the dominant phylum of diderm bacteria in the distal gut, are not known to produce siderophores. *Bacteroides thetaiotaomicron* (*B. theta*) has been shown to prefer haem-bound iron over soluble ferrous iron[16]. *B. theta* likely acquires haem from the diet[17] as well as from dead intestinal cells and dead bacteria. It was recently shown that during *Salmonella* spp. infection in the mouse gut, when iron availability becomes limiting, *B. theta* upregulates a novel iron uptake system that steals iron-laden siderophores produced by the pathogenic *Salmonella*[18]. This xenosiderophore (i.e., foreign siderophore) utilization system (Xus) consists of the TonB-dependent transporter XusA, the surface-exposed lipoprotein XusB and a PepSY domain-containing inner membrane protein XusC[18,19]. The XusABC system provides resilience to *B. theta* during infection, but secreted FeEnt-bound XusB also acts as an iron reservoir for the pathogen[18,19]. It is therefore important to understand the molecular details of this iron piracy system to obtain a deeper understanding of pathogen-symbiont interactions inside the gut.

Here, we present crystal structures of the XusB lipoprotein by itself and in complex with FeEnt, which reveal the mechanism of xenosiderophore capture. We also use single particle cryo-EM to investigate how XusB interacts with the XusA TonB-dependent transporter. Our structural bioinformatics analysis reveals substantial variability in xenosiderophore utilization systems in Bacteroidetes. Together, our results provide mechanistic insights into catecholate xenosiderophore uptake across the OM of *B. theta* and suggest potential new functions for homologous systems.

Results

Crystal structures of apo and FeEnt-bound XusB

We expressed recombinant *B. theta* XusB lacking the signal sequence and the lipid anchor cysteine in *E. coli* BL21(DE3) and determined its crystal structure at 1.5 Å (Figure 1a and b, Supplementary Table 1). XusB has a seven-bladed β-propeller fold with a distinct 15-residue loop, which we term the hook, inserted into the β2 blade that sticks outwards from the β-propeller (Figure 1a). The β-propeller pocket (Figure 1b) has been suggested to bind FeEnt based on computational docking[19].

We co-crystallized recombinant XusB with FeEnt and determined the crystal structure of the complex at 1.7 Å. XusB binds FeEnt via four loops (Figure 1c), including the hook. Interestingly, FeEnt binds off the β-propeller pocket rather than inside it, and the distance to the previously modelled binding site[19] is ~10 Å (Figure 1d). The FeEnt electron density in the co-crystal structure was of very high quality (Figure 1e), with the cyclic triserine lactone, amide linkers and Fe^{3+}-ligating catecholate groups fully resolved. We observed that the catecholate arms of FeEnt are not perpendicular to the triserine lactone ring plane but slanted to one side (Figure 1e, Supplementary Movie 1), in agreement with the structure of FeEnt in isolation[4]. FeEnt does not undergo conformational changes upon binding to XusB. Instead, XusB loops close in on FeEnt, forming a 418.8 $Å^2$ interaction interface (Supplementary Figure 1 and 2, Supplementary Movie 2). All three catecholate arms of FeEnt interact with XusB loops L1-4 (Figure 1c and f). Sidechains of N120, R167 and Q413 slot between the slanted catecholate arms, while S121, S168 and Y411 sidechains form hydrogen bonds with the *meta* oxygens of the catecholate groups (Figure 1f, Supplementary Movie 1). One amide linker of FeEnt hydrogen bonds to a single water molecule, another to a water molecule and the sidechain of Q413, and the third to the sidechain of R255 (Figure 1f). The sidechain of R167 possibly forms a hydrogen bond with the triserine lactone ring—the only interaction between XusB and this part of FeEnt.

The binding affinity of FeEnt to XusB was determined by isothermal titration calorimetry (ITC) to be approximately 60 nM (Figure 1g). To confirm the observed binding site, we constructed a XusB variant, $XusB^{R167A,\Delta hook}$, with the R167A substitution and deletion of residues 119-122 which form the tip of the hook. $XusB^{R167A,\Delta hook}$ did not bind FeEnt (Figure 1g), indicating that the binding site observed in the co-crystal structure is the only FeEnt binding site on XusB.

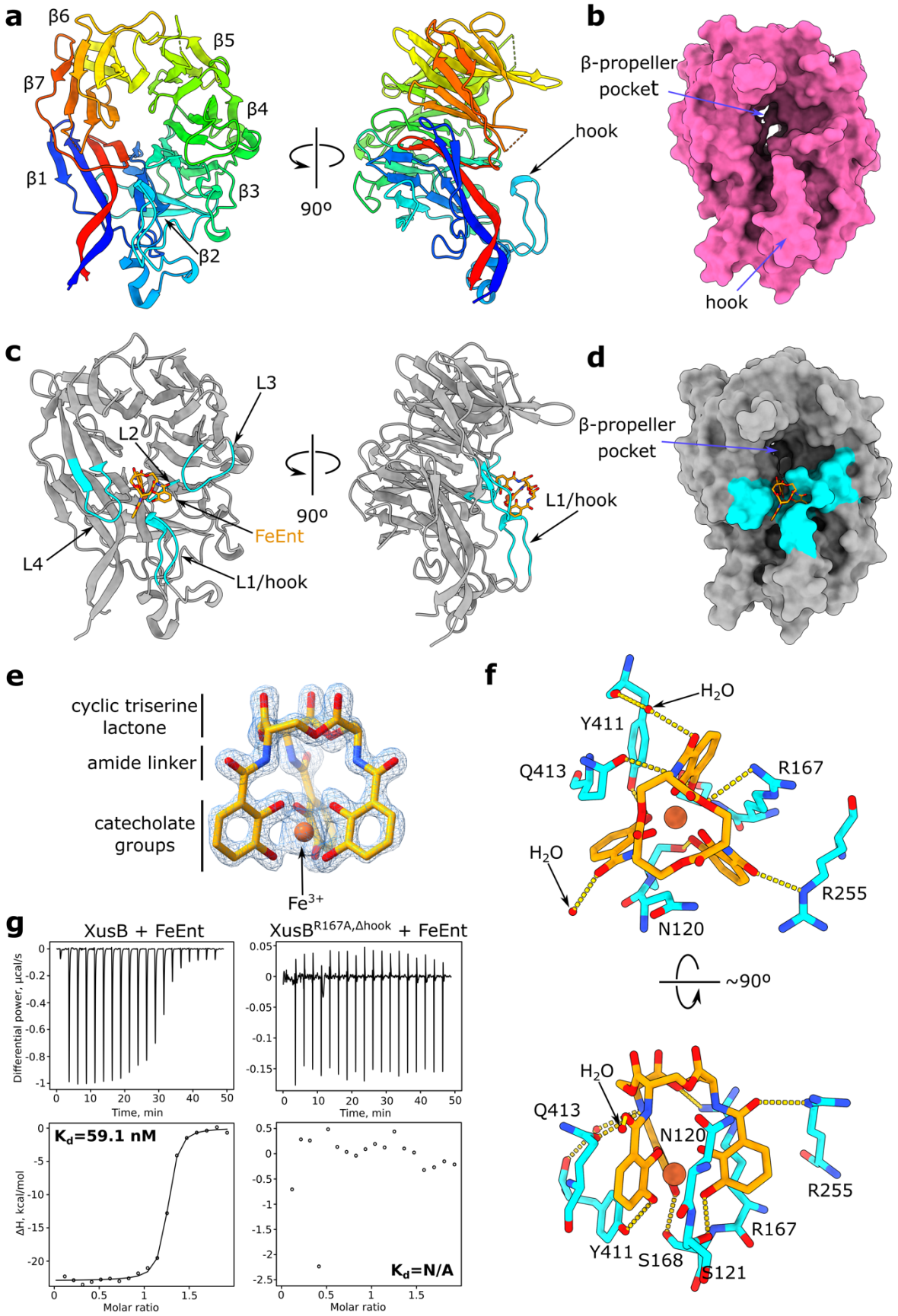

Figure 1. XusB xenosiderophore binding properties. (**a**) Crystal structure of apo XusB at 1.5 Å. The cartoon is coloured in rainbow; the N-terminus is blue, the C-terminus is red. Blades of the

β-propeller (β1-7) are labelled starting from the N-terminus. (**b**) Surface representation of apo XusB. (**c**) Co-crystal structure of XusB bound to FeEnt at 1.7 Å. FeEnt is depicted as an orange stick model. The four FeEnt binding loops (L1-L4) are shown in cyan. (**d**) Surface representation of XusB bound to FeEnt. (**e**) FeEnt model fit into the 2mFo-DFc electron density map at 2σ. (**f**) XusB residues interacting with FeEnt. The yellow dashed lines show likely hydrogen bonds. N120, S121 – L1/hook; R167, S168 – L22; R255 – L3; Y411, Q413 – L4. (**g**) Representative isothermal titration calorimetry experiments where 250 μM FeEnt was titrated into 25 μM XusB (left) or 25 μM $XusB^{R167A,\Delta hook}$ variant (right). Integrated heats were fitted to a single binding site model, giving the indicated Kd value for the XusB-FeEnt titration; no K_d value could be determined for the $XusB^{R167A,\Delta hook}$ titration.

Cryo-EM structure of native XusAB complex

FeEnt is sufficient to rescue growth of *B. theta* under iron limiting conditions (Supplementary Figure 3). We reasoned that the proteins encoded by the Xus operon would be expressed to high enough copy number for purification and structural characterisation if the cells were cultured under iron-limiting conditions. We purified the native XusAB complex from the *B. theta bt2064-his* strain grown in minimal medium supplemented with the iron chelator bathophenanthroline disulfonate (BPS) (Supplementary Figure 3, Methods). We determined the structure of XusAB by single particle cryo-EM to a global resolution of 2.7 Å, with local resolution extending to 2.2 Å (Figure 2a, Supplementary Figure 4, Supplementary Table 2). The resolved portion of XusA has a classic TonB-dependent transporter fold: a micelle-embedded 22-strand β-barrel plugged via an N-terminal plug domain[2]. The XusA (UniProt Q8A621) extreme N-terminal carboxypeptidase-like domain of unknown function was not resolved in our structure likely because it is connected to the barrel via flexible linker. The conformation of XusB in the XusAB complex is similar to that observed in the apo XusB crystal structure, with Cα-Cα RMSD = 0.9 Å. We did not observe any alternative conformations, sub-complexes or movement of XusA and XusB in the cryo-EM data.

XusB sits on top of the extracellular side of XusA like a lid, reminiscent of *B. theta* TonB-dependent transporter and surface-exposed lipoprotein complexes that take up glycans and vitamin B_{12}[20,21]. The interaction interface of XusA and XusB is extensive: PISA analysis indicates 52 hydrogen bonds and 6 salt bridges, with a total interaction surface area of 2,794.6 $Å^2$ (Supplementary Figure 5). XusB interacts with every single extracellular loop of XusA, except for the loop between barrel strands β9 and β10, which is disordered (Figure 2b). Although we did not observe FeEnt in the cryo-EM structure, the XusB hook facing towards a cavity enclosed by the XusAB complex (Figure 2a and b) indicates that FeEnt binds inside this cavity. We speculate that XusB moves in a hinge-like motion opening and closing the XusAB cavity like a lid, thus transiently allowing extracellular xenosiderophores access to their binding site on the inward-facing side of XusB.

XusB binds FeEnt with reasonably high affinity (Figure 1g), but FeEnt must somehow be transferred from XusB to XusA to achieve transport across the OM. Structural alignment of the cryo-EM XusB structure and the XusB-FeEnt co-crystal structure reveals that Q413, part of L4, must undergo a shift of 7.7 Å to interact with FeEnt (Figure 2c). However, the position of L4 in the XusB-FeEnt structure would result in clashes with the XusA β7-8 extracellular loop within the apo complex (Figure 2d). Furthermore, L4 in the apo complex

is stabilised via a salt bridge between E416 and K354 of XusA β5-6 extracellular loop. This suggests that the FeEnt-bound state of XusB when in complex with XusA might be short-lived despite the high affinity of XusB for FeEnt. This is because the XusA β7-8 extracellular loop would displace L4 of XusB, aided by formation of the E416-K354 salt bridge, thus disrupting the FeEnt binding pocket and releasing the xenosiderophore to diffuse towards XusA, which would transport it across the OM.

We observed unexplained density extending from the sidechain of T401, which is part of the XusA β7-8 extracellular loop (Supplementary Figure 6). Together with flanking residues this threonine forms a DTA sequence, which matches the Bacteroidetes O-glycosylation motif[22]. We therefore conclude that the cryo-EM density extending from T401 corresponds to a glycan chain. Four sugar units can be discerned, including the branching deoxyhexose previously identified in the *B. fragilis* O-glycan[23]. The T401 glycosylation site is located near residues 421-423 which are implicated in FeEnt release from XusB (Figure 2d and Supplementary Figure 6). The sidechain of T401 and the O-glycan face the solvent rather than XusB, but we cannot rule out that the glycan modification affects the conformation of neighbouring XusA extracellular loops and that it could be functionally important.

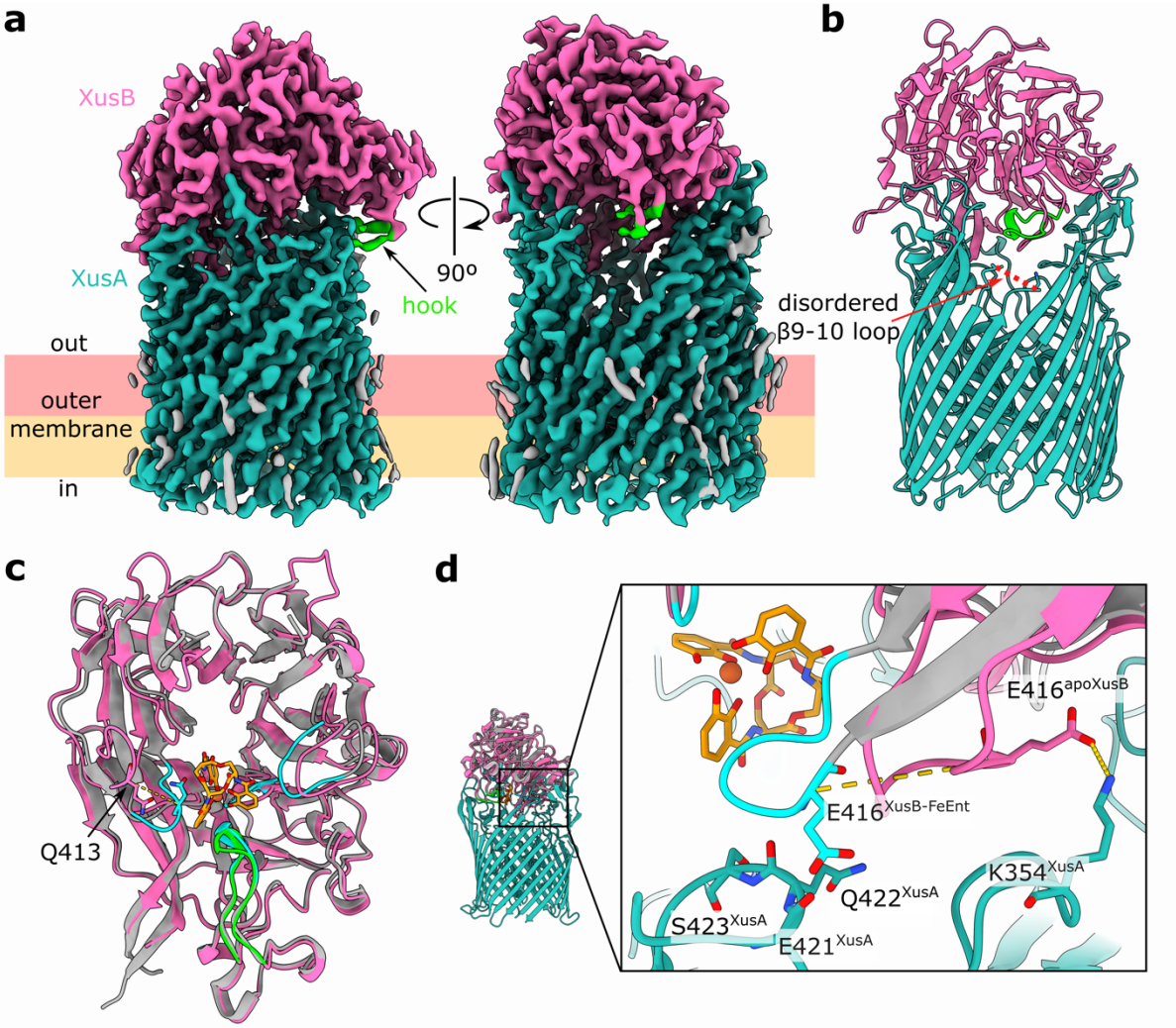

Figure 2. Cryo-EM structure of the native XusAB complex. (**a**) Single particle cryo-EM reconstruction of the XusAB complex at 2.7 Å global resolution. (**b**) Model built into the cryo-EM

density in cartoon representation. The red dashed line depicts the disordered extracellular loop between β strands 9 and 10 of the XusA β-barrel, corresponding to residues 464-473. (**c**) Structural alignment of the apo-XusB structure observed in the cryo-EM reconstruction (hot pink, hook loop in green) and the XusB-FeEnt co-crystal structure (grey, FeEnt binding loops in cyan). Cα-Cα RMSD = 1.6 Å. The dashed yellow line corresponds to a distance of 7.7 Å between the Cα atoms of Q413, which is part of the L4 FeEnt binding loop, observed in the two structures. (**d**) Close-up view of XusB L4 in the apo cryo-EM structure and the XusB-FeEnt co-crystal structure, viewed from a different orientation compared to (**c**). Colouring as in (**c**), XusA is in light sea green. The large yellow dashes correspond to a distance of 11.3 Å between the Cα atoms of E416 in the two structures. The small yellow dashes show a salt bridge between K354 of XusA and E416 of XusB in the cryo-EM structure. Residues E421, Q422 and S423 are part of the β7-8 extracellular loop of XusA.

Structural variety of XusB homologues

B. theta XusB (UniProt Q8A622) is annotated as a DUF4374 domain-containing protein, which takes on a β-propeller fold as demonstrated by structural data. We investigated the predicted structures of DUF4374 domain-containing homologues. The top hits from protein BLAST searches of the *B. theta* XusB sequence against Bacteroidetes genomes have a sequence identity of around 60%. The reason for the low sequence identity for the top BLAST hits is that the *B. theta* XusB hook position inside the β2 propeller blade is unique (Figure 3a). Other Bacteroidetes XusB homologues such as *Parabacteroides distasonis* BDI_3402 (59.52% identity) and *Barnesiella viscericola* BARVI_05925 (43.36% identity) are predicted to have their hook inserted in the β4 blade or, in the case of *B. fragilis* BF9343_4228 (20.21% identity), do not appear to have a hook at all (Figure 3b-d and Supplementary Figure 7). These DUF4374 domain-containing proteins are likely part of genuine xenosiderophore utilization systems, rather than performing some other function. They all contain a lipoprotein export signal that directs proteins to the outer leaflet of the OM[24]. Additionally, they are encoded next to TonB-dependent transporters and PepSY domain-containing inner membrane proteins that likely reduce siderophore-bound ferric iron to facilitate dissociation of the iron-siderophore complex[25] (Figure 3e). *P. distasonis* also encodes a periplasmic esterase (BDI_3403) in the same operon as the XusB homologue which might might liberate siderophore-bound iron via hydrolysis of the triserine lactone ring, as shown for FeEnt in *E. coli*[7,8].

Conservation of the hook and L2 amino acid sequences between the *B. theta, P. distasonis* and *B. viscericola* homologues (Supplementary Figure 7) suggests that, despite differences in position of the hook within the β-propeller, *P. distasonis* and *B. viscericola* XusB might still bind FeEnt or perhaps structurally similar catecholate siderophores. However, the *B. fragilis* homologue is unlikely to bind FeEnt due to lack of all FeEnt-binding regions observed in the XusB-FeEnt co-crystal structure, which is consistent with a previous report that *B. fragilis* cannot utilize iron bound to catecholate siderophores[26].

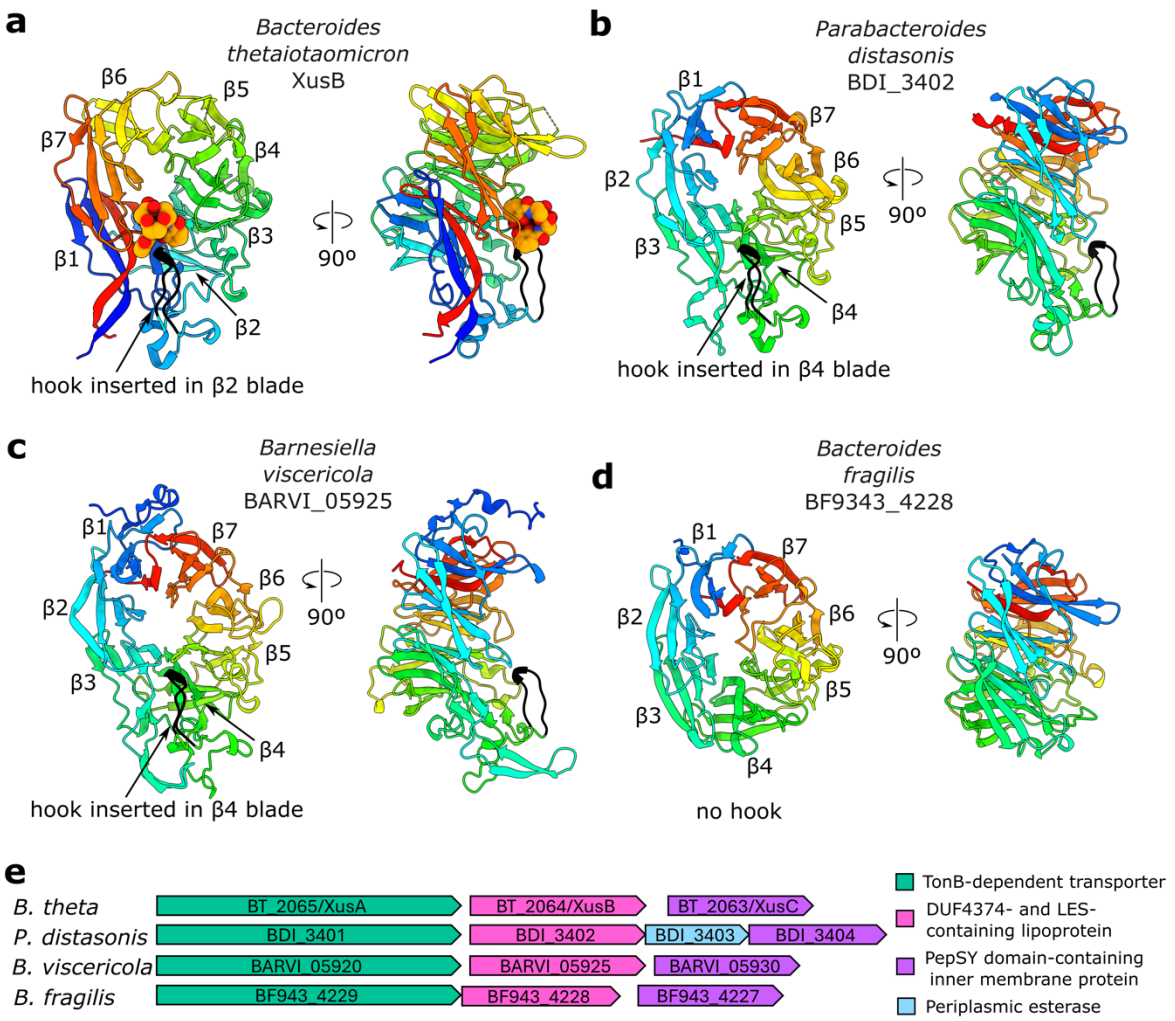

Figure 3. Structural variety of DUF4374 domain proteins. (**a**) *B. theta* XusB-FeEnt co-crystal structure. FeEnt atoms are displayed as spheres. (**b**) *P. distasonis* DSM 20701 BDI_3402 (59.52% identity to *B. theta* XusB), (**c**) *B. viscericola* DSM 18177 BARVI_05925 (43.36% identity to *B. theta* XusB), and (**d**) *B. fragilis* NCTC 9343 BF9343_4228 (20.21% identity to *B. theta* XusB) AlphaFold2[27] models. Views were generated from a superposition, β-propeller blades are labelled β1-7 starting from the N-terminus. All models are coloured in rainbow, from the N-terminus in blue to the C-terminus in red; the hook is in black. AlphaFold2 model prediction confidence is shown in Supplementary Figure 8. (**e**) Genetic context of the selected XusB homologues. DUF, domain of unknown function; LES, lipoprotein export signal[24].

Discussion

There are many TonB-dependent transporters in Bacteroidetes that transport unknown molecules[28]. We must understand what these transporters are transporting and how, so that we can obtain a more complete understanding of microbial interactions inside the gut. Our structures show how a Bacteroidetes TonB-dependent transporter-lipoprotein complex takes up xenosiderophores and contribute to the ever-widening substrate range described for lipoprotein-assisted TonB-dependent transporters[2,20,21,28–30].

We observed an excess of XusB in our native XusAB purifications (Supplementary Figure 3). The excess XusB is likely destined for secretion in outer membrane vesicles (OMVs)[19].

It has been shown that OMVs containing FeEnt-loaded XusB can be used as an iron source by *B. theta*[19]. This implies that the OMVs can somehow deliver FeEnt-XusB to XusA in the OM of recipient bacteria. However, our cryo-EM structure shows that XusAB form a tight, closed complex even in the absence of FeEnt. It is unclear how FeEnt-bound XusB could displace the apo-XusB bound to XusA. We speculate that XusB transiently opens like a lid and gives access to the XusAB cavity to incoming xenosiderophores. Alternatively, the disordered β9-10 extracellular loop of XusA acts as a lateral gate for ingress of xenosiderophores. The latter hypothesis is favoured by lack of any XusAB particles in an open state in the cryo-EM data. On the other hand, closure of a mobile XusB lid appears more effective in dislodging the XusB-bound siderophore via clashes with XusA loop β7-8, and we therefore favour the hypothesis of a mobile XusB lid delivering the xenosiderophore to the XusA transporter. It is interesting that, while open lipoprotein lids have been observed experimentally for all characterised dimeric SusCD transporters[21,29,30], for unknown reasons this has not been the case for BtuBG[20] and XusAB systems, which are all monomeric. It is also unclear why we could not load the purified XusAB complex with FeEnt. The in vitro conditions may somehow preferentially stabilise the complex in a closed state. It is also conceivable that excess free, but OM-anchored XusB plays a role in complex opening.

XusAB can transport at least two structurally similar xenosiderophores, FeEnt and its diglucosylated form, salmochelin[18,26]. XusB predominately interacts with the triscatecholate structure of FeEnt and, from inspection of the structure, the binding site appears to be able to accommodate the two glucosyl groups of salmochelin. Furthermore, the triserine lactone of FeEnt is exposed to solvent and forms only one contact with XusB, suggesting that the binding site could accommodate siderophores with different backbones connecting the catecholate arms and raising the question of how many different siderophores the *B. theta* XusABC system can utilize.

B. theta XusB appears to be unique in terms of the hook position in the β2 blade, while in other Bacteroidetes the hook is inserted in the β4 blade—do these homologues still bind FeEnt? It has been reported that while *B. theta* can utilize catecholate xenosiderophores it cannot take up ferrichrome, a hydroxamate siderophore; the opposite is true for *B. fragilis*[26]. *B. fragilis* XusB does not have the hook at all, suggesting that it might be binding xenosiderophores with different iron-chelating groups, such as ferrichrome. If that is indeed the case, how many Xus systems dedicated to different siderophores are there in the rest of the Bacteroidetes phylum?

Methods

Bacterial strains and culture conditions

E. coli BL21(DE3) and TOP10 strains were genetically manipulated using standard laboratory procedures. The kanamycin concentration used in liquid and solid lysogeny broth (LB) was 50 μg/ml. *B. theta* VPI-5482 *tdk*$^-$ was cultured either in brain-heart infusion (BHI, Oxoid) supplemented with 1 μg/ml haemin or defined minimal medium[31] supplemented with 1 μg/ml haemin and 0.5% fructose. *B. theta* was grown under

anaerobic conditions at 37°C in a Don Whitley A35 workstation. When required, 200 µg/ml gentamycin and 25 µg/ml erythromycin was used for selection of *B. theta*.

Construction of expression plasmids

The nucleotide sequence coding for amino acid residues 24-464 of XusB (*bt_2064*), which excludes the signal sequence and the lipid anchor cysteine, was amplified by PCR using *B. theta* genomic DNA as the template and primers that introduce overhangs containing restriction sites. The PCR product was digested with NcoI and XhoI FastDigest restriction enzymes (ThermoFisher Scientific) and ligated into pET28b, resulting in a C-terminal His_6-tag fusion. The $XusB^{R167A,\Delta hook}$ binding site variant nucleotide sequence with flanking NcoI and XhoI restriction sites was synthesised and ligated into the pTwist Amp High Copy plasmid by Twist Bioscience. The synthetic DNA sequence was sub-cloned into pET28b using the flanking restriction sites. Cloning was carried out in *E. coli* TOP10 cells. Clones were screened for successful insert ligation by colony PCR using EmeraldAmp GT PCR master mix (Takara Bio) with T7 promoter and T7 terminator primers. All constructs were verified by Sanger sequencing (Eurofins).

Protein expression and purification in *E. coli*

E. coli BL21(DE3) cells were transformed with plasmids carrying the coding sequences for soluble variants of XusB, plated on LB kanamycin agar plates and incubated at 37°C overnight. The following day, approximately one third of transformants were scraped off the agar plate and used to start an LB kanamycin preculture, which was incubated at 37°C with shaking for 1.5-3 hours. 12-15 ml of preculture was used to inoculate 1 litre flasks of pre-warmed LB kanamycin medium. The cultures were incubated at 37 °C with shaking until optical density at 600 nm reached 0.4-0.8. Protein expression was then induced by adding 0.1 mM isopropyl β-d-1-thiogalactopyranoside, and the cultures were grown for another 16-20 h at 18 °C with 150 rpm shaking. Cells were harvested by centrifugation at 8,000*g* at 4 °C for 20 min. Pellets were resuspended in cold Tris-buffered saline (TBS, 20 mM Tris-HCl, 300 mM NaCl) and stored at -20 °C until protein purification. Cell pellets were thawed and homogenized in TBS using a Dounce tissue grinder, and supplemented with DNase I (Roche). Cells were lysed by passing the suspension once through a cell disruptor (Constant Systems) at 20 kpsi. The lysates were supplemented with 1 mM phenylmethylsulfonyl fluoride (PMSF) and clarified by centrifugation at 30,000*g* for 30 min at 4 °C. The supernatants were loaded on 5 ml chelating Sepharose columns charged with Ni^{2+} ions using gravity flow. The columns were washed with 30 column volumes of TBS with 30 mM imidazole. Bound proteins were eluted with 4 column volumes of TBS with 250 mM imidazole. The eluate was concentrated with an Amicon Ultra filtration device (30 kDa cut-off membrane), loaded on a HiLoad Superdex 200 16/600 pg column and eluted in 10 mM HEPES-NaOH pH 7.5, 100 mM NaCl. Fractions were analysed by SDS-PAGE. Fractions containing the soluble XusB variants were pooled, concentrated, flash-frozen and stored at -80 °C.

Preparation of ferric enterobactin

Iron-free enterobactin was dissolved in dimethyl sulfoxide (DMSO) to make a 10 mM solution. The 10 mM enterobactin DMSO solution was mixed in a 1:1 volume ratio with 10 mM aqueous $FeCl_3$ solution, to yield a 5 mM FeEnt stock solution in 50% (v/v) DMSO. The exact concentration of FeEnt was determined spectrophotometrically using the

extinction coefficient ε_{495} = 5,600 M^{-1} cm^{-1}. The stock solution was stored in small aliquots at -80ºC to minimise enterobactin hydrolysis.

Crystal structure determination

The purified soluble XusB variant was concentrated to 36 mg/ml. Sitting drop vapour diffusion crystallisation screens were set up using a Mosquito robot (SPT Labtech) either with apo XusB or with a 1:1.1 molar ratio of XusB and FeEnt. The crystallization plates were incubated at 20°C. Apo XusB crystals appeared after less than a week in the PACT premier screen (Molecular Dimensions) containing 0.1 M MES pH 6.0, 0.2 M calcium chloride and 20% PEG 6000. Crystals were cryo-protected in mother liquor supplemented with ~20% PEG 400 and flash-cooled in liquid nitrogen. XusB-FeEnt co-crystals appeared in the Index screen (Hampton Research) condition containing 0.1 M citric acid pH 3.5 and 2 M ammonium sulphate after 2 weeks. Crystals were cryo-protected by passing through a drop of 3.5 M ammonium sulphate and flash-cooled in liquid nitrogen.

X-ray diffraction data were collected at the Diamond Light Source synchrotron (UK) at a temperature of 100 K (Supplementary Table 1). Data was processed with XIA2[32], scaled with Aimless[33], and the space group was confirmed with Pointless[34]. The apo XusB structure was solved by molecular replacement using an AlphaFold2[27] predicted model. The apo XusB model was used to phase the XusB-FeEnt diffraction dataset by molecular replacement. The models underwent cycles of manual building in Coot[35] and refinement in Phenix[36] until no further improvement in R factors could be achieved. The models were validated using MolProbity[37]. Refinement statistics are summarised in Supplementary Table 1.

Isothermal titration calorimetry

ITC was carried out in 10 mM HEPES–NaOH pH 7.5 and 100 mM NaCl supplemented with 5% DMSO to improve FeEnt solubility. A 250 μM FeEnt solution was made in ITC buffer, and any precipitate was removed by centrifugation. The clarified FeEnt solution was titrated into 25 μM protein at 25°C using a Microcal PEAQ-ITC instrument (Malvern Panalytical). After an initial delay of 60 s, a single injection of 0.4 μl was carried out, which was discarded from data analysis, followed by 18 injections of 2 μl spaced in 150 s intervals. The sample cell was stirred at 750 rpm during titration. Ligand to buffer control titrations were subtracted from all experiments. The experiments were repeated at least twice. Data were fitted to a single-binding-site model using the Microcal PEAQ-ITC Analysis software v1.40.

Growth curve experiments

B. theta tdk$^-$ strain was cultured anaerobically in BHI supplemented with haemin at 37ºC overnight. 0.2 ml of the overnight culture was used to inoculate 5 ml of fresh supplemented BHI the next morning, followed by a 4 h incubation. The cells were collected by centrifugation for 5 min at 2,800*g*, 20ºC, and resuspended in 1 ml of fresh, pre-warmed minimal medium. Minimal medium supplemented with fructose and haemin was aliquoted into tubes, to which BPS, FeEnt and $FeCl_3$ was added as required. Washed cells were diluted in the appropriate tubes to OD_{600}=0.04 and dispensed in 200 μl aliquots into the wells of a sterile 96-well plate in triplicate. Growth at 37ºC was

monitored for 48 h using a Biotek Epoch microplate reader housed inside an anaerobic workstation. The experiment was repeated three times with similar results.

Purification of the XusAB complex from *B. theta*

A C-terminal His_6-tag was fused to XusB by introducing the tag coding sequence into the *B. theta tdk*$^-$ chromosome before the stop codon of *bt_2064* via allelic exchange using the pExchange plasmid[38]. Presence of the tag on the chromosome was confirmed by PCR and Sanger sequencing. Conditions under which the tagged XusB is expressed were identified by Western blotting. The *B. theta bt_2064-his* strain was cultured anaerobically in tubes containing 2 ml minimal medium supplemented with 6.25-100 μM BPS for 18 h. Equivalents of 1 ml culture at OD_{600}=2 were pelleted by centrifugation. The pellets were resuspended in 80 μl BugBuster (Sigma), supplemented with 1 mM PMSF, and incubated for 15 min at room temperature. Cell debris was pelleted by centrifugation in a benchtop microcentrifuge. Samples from cells grown in the presence of different amounts of BPS were separated by SDS-PAGE and transferred onto a PVDF membrane via wet transfer. The PVDF membrane was stained with Ponceau S stain to confirm successful transfer and blocked with 1% milk solution in PBS supplemented with 0.1% (v/v) Tween 20 for 20 min at room temperature. The membrane was probed with anti-His-horseradish peroxidase conjugate antibody (1:500 dilution in 1% milk solution) for 1 h at room temperature and washed three times with PBS-Tween. The blots were developed using SuperSignal West Pico Plus chemiluminescent substrate (Thermo Fisher Scientific) and imaged using a Gel Doc XR+ system (Bio-Rad).

Stabs of *B. theta bt_2064-his* glycerol stocks were used to inoculate BHI, followed by overnight incubation at 37°C under anaerobic conditions. After autoclaving, minimal medium was stored in an A35 Don Whitley anaerobic workstation overnight. The following day, the minimal medium was supplemented 50 μM BPS, fructose (0.5%) and haemin (1 μg/ml). Overnight *B. theta* BHI cultures were pelleted, resuspended in minimal medium to original volume and used to inoculate 0.5 litre bottles of minimal medium at a ratio of 1:250. Bacteria were cultured at 37 °C under anaerobic conditions for 18-20 h. Cultures were pelleted by centrifugation at 6,000g for 30 min at 4 °C, resuspended in TBS, and stored at -20 °C.

Pellets were thawed, supplemented with DNase I and homogenised. Cells were lysed by passing the cell suspension once through a cell disruptor at 22 kpsi. The lysate was clarified by centrifugation at 30,000 × g, 4 °C for 30 min. Membranes were isolated from the clarified lysate by ultracentrifugation at 140,000 × g, 4 °C for 50 min, followed by solubilization in 1.5% lauryldimethylamine N-oxide (LDAO) in TBS for 1 h at 4 °C. Insoluble material was pelleted by centrifugation at 44,000 × g, 4 °C for 30 min. The solubilised material was passed through ~3 ml of chelating Sepharose resin charged with Ni^{2+} ions using gravity flow. The column was washed with 25 column volumes of TBS with 30 mM imidazole and 0.1% dodecyl-β-D-maltopyranoside (DDM, Anatrace), and bound protein was eluted with TBS supplemented with 200 mM imidazole and 0.03% DDM. The eluate was concentrated using an Amicon Ultra filtration device (100 kDa cut-off membrane), loaded on a Superdex 200 10/300 Increase column and eluted in 10 mM

HEPES-NaOH pH 7.5, 100 mM NaCl, 0.03% DDM. Fractions corresponding to the XusAB peak were pooled, concentrated, flash-frozen in liquid nitrogen, and stored at −80 °C.

Cryo-EM structure determination

Pure XusAB complex at 7 mg/ml was incubated with a four-fold molar excess of FeEnt for 45 min at room temperature. 3.5 µl of the complex was then applied to glow-discharged Quantifoil R1.2/1.3 copper 200 mesh holey carbon grids. The grids were immediately blotted for 1-5 s and plunge-frozen in liquid ethane using a Vitrobot Mark IV (ThermoFisher Scientific) device operating at 4 °C and 100% humidity. The grids were initially screened on a FEI Glacios microscope at the University of York (UK). Data were collected at the Astbury Centre (Leeds, UK) on a FEI Titan Krios microscope operating at 300 kV using a Falcon 4i direct electron detector (ThermoFisher Scientific) operating in counting mode (Supplementary Table 2). A total of 6,645 movies were recorded in electron event representation (EER) format at 165k magnification, corresponding to a pixel size of 0.74 Å.

The cryo-EM workflow is shown in Supplementary Figure 4. All data processing was done in cryoSPARC v4.4.1. Movies were motion-corrected using patch motion correction. CTF parameters were fitted using patch CTF correction. Initially, ~2,000 particles were picked manually and used to make 2D classes for template picking. 1,110,843 picked particles were extracted in 480-pixel boxes (0.74 Å/pixel), Fourier cropped to a box size of 240 pixels (1.48 Å/pixel) and subjected to two rounds of 2D classification. Ab initio models were generated from classes exhibiting protein density and decoy models were generated from classes containing predominately noise. Particles selected after 2D classification were subjected to heterogeneous refinement against four ab initio models, two of which were decoys. A single class from heterogeneous refinement refined to high resolution in non-uniform refinement[39]. Most particles clustered into a single class in 3D classification (8 classes in total). Particles from this class were re-extracted in 480-pixel boxes (0.74 Å/pixel) and refined using non-uniform refinement (per-particle defocus, tilt and trefoil refinement enabled), followed by local refinement. Per-particle motion correction was performed using reference-based motion correction, followed by local refinement and re-estimation of per-particle defocus, tilt and trefoil parameters. The particle stack was subjected to a final round of 2D classification with the noise model (sigma) annealing turned off to remove any remaining poor-quality particles. Another round of reference-based motion correction was performed, followed by a final round of local refinement that gave a map with a global resolution of 2.7 Å based on the FSC=0.143 criterion. The final stack had 76,979 particles.

The XusAB protein sequences were supplied to ModelAngelo[40] for automated model building. The resulting model was iteratively adjusted in Coot[35] and ISOLDE[41] and refined using Phenix real space refinement[36]. The model was validated using MolProbity[37]. Refinement statistics are shown in Supplementary Table 2.

Structure analysis and visualisation

Atomic models, electron density maps and cryo-EM maps were analysed in Coot[35] and UCSF ChimeraX[42]. All figures depicting structural data were generated using UCSF ChimeraX. The ISOLDE[41] plugin was used to visualise electron density maps.

Data availability

Atomic coordinate files, electron microscopy volumes and source data will be made publicly available upon publication of this manuscript.

Author contributions

A.S. designed experiments, made constructs, purified and crystallized proteins, made cryo-EM grids and collected cryo-EM data, determined crystal and cryo-EM structures, and wrote the manuscript with input from B.v.d.B. Y.L.S. and H.M. made expression constructs, purified and crystallized proteins, and carried out ITC titrations, supervised by A.S. and B.v.d.B. A.B. collected X-ray diffraction data and provided computational support. B.v.d.B. acquired funding, designed experiments, and collected cryo-EM data.

Acknowledgements

We thank Matthew Nodwell (Simon Fraser University) for providing the enterobactin used in this study. We also thank Diamond Light Source for access to macromolecular crystallography beamlines (proposal mx-24948). We acknowledge use of the crystallization facilities and the GPU cluster for cryo-EM data processing at the Newcastle Structural Biology Laboratory. We acknowledge use of the Glacios microscope for screening cryo-EM grids at the York Structural Biology Laboratory (University of York). We acknowledge use of the Astbury Centre (University of Leeds) Titan Krios microscope. This work was supported by a Wellcome Trust Investigator award (214222/Z/18/Z) to B.v.d.B, providing salary support to A.S.

Ethics declarations

The authors declare no competing interests.

References

1. Andrews, S. C., Robinson, A. K. & Rodríguez-Quiñones, F. Bacterial iron homeostasis. *FEMS Microbiol Rev* **27**, 215–237 (2003).
2. Silale, A. & Van Den Berg, B. TonB-Dependent Transport Across the Bacterial Outer Membrane. *Annu Rev Microbiol* **77**, 67–88 (2023).
3. Raymond, K. N., Dertz, E. A. & Kim, S. S. Enterobactin: An archetype for microbial iron transport. *Proc Natl Acad Sci U S A* **100**, 3584–3588 (2003).
4. Johnstone, T. C. & Nolan, E. M. Determination of the Molecular Structures of Ferric Enterobactin and Ferric Enantioenterobactin Using Racemic Crystallography. *J Am Chem Soc* **139**, 15245–15250 (2017).
5. Annamalai, R., Jin, B., Cao, Z., Newton, S. M. C. & Klebba, P. E. Recognition of ferric catecholates by FepA. *J Bacteriol* **186**, 3578–3589 (2004).
6. Buchanan, S. K. *et al.* Crystal structure of the outer membrane active transporter FepA from Escherichia coli. *Nature Structural Biology 1999 6:1* **6**, 56–63 (1999).

7. Brickman, T. J. & McIntosh, M. A. Overexpression and purification of ferric enterobactin esterase from Escherichia coli. Demonstration of enzymatic hydrolysis of enterobactin and its iron complex. *Journal of Biological Chemistry* **267**, 12350–12355 (1992).
8. O'Brien, I. G., Cox, G. B. & Gibson, F. Enterochelin hydrolysis and iron metabolism in Escherichia coli. *Biochimica et Biophysica Acta (BBA) - General Subjects* **237**, 537–549 (1971).
9. Murdoch, C. C. & Skaar, E. P. Nutritional immunity: the battle for nutrient metals at the host–pathogen interface. *Nature Reviews Microbiology 2022 20:11* **20**, 657–670 (2022).
10. Miethke, M. & Marahiel, M. A. Siderophore-Based Iron Acquisition and Pathogen Control. *Microbiology and Molecular Biology Reviews* **71**, 413–451 (2007).
11. Kramer, J., Özkaya, Ö. & Kümmerli, R. Bacterial siderophores in community and host interactions. *Nature Reviews Microbiology 2019 18:3* **18**, 152–163 (2019).
12. Coyte, K. Z. & Rakoff-Nahoum, S. Understanding Competition and Cooperation within the Mammalian Gut Microbiome. *Current Biology* **29**, R538–R544 (2019).
13. Huttenhower, C. *et al.* Structure, function and diversity of the healthy human microbiome. *Nature 2012 486:7402* **486**, 207–214 (2012).
14. Coe, G. L. *et al.* Dynamic Gut Microbiome Changes in Response to Low-Iron Challenge. *Appl Environ Microbiol* **87**, 1–14 (2021).
15. Celis, A. I., Relman, D. A. & Huang, K. C. The impact of iron and heme availability on the healthy human gut microbiome in vivo and in vitro. *Cell Chem Biol* **30**, 110-126.e3 (2023).
16. Meslé, M. M., Gray, C. R., Dlakić, M. & DuBois, J. L. Bacteroides thetaiotaomicron, a Model Gastrointestinal Tract Species, Prefers Heme as an Iron Source, Yields Protoporphyrin IX as a Product, and Acts as a Heme Reservoir. *Microbiol Spectr* **11**, (2023).
17. Martínez-Navarrete, N., Camacho, M. M., Martínez-Lahuerta, J., Martínez-Monzó, J. & Fito, P. Iron deficiency and iron fortified foods—a review. *Food Research International* **35**, 225–231 (2002).
18. Zhu, W. *et al.* Xenosiderophore Utilization Promotes Bacteroides thetaiotaomicron Resilience during Colitis. *Cell Host Microbe* **27**, 376-388.e8 (2020).
19. Spiga, L. *et al.* Iron acquisition by a commensal bacterium modifies host nutritional immunity during Salmonella infection. *Cell Host Microbe* **31**, 1639-1654.e10 (2023).
20. Abellon-Ruiz, J. *et al.* BtuB TonB-dependent transporters and BtuG surface lipoproteins form stable complexes for vitamin B12 uptake in gut Bacteroides. *Nature Communications 2023 14:1* **14**, 1–18 (2023).
21. White, J. B. R. *et al.* Outer membrane utilisomes mediate glycan uptake in gut Bacteroidetes. *Nature 2023 618:7965* **618**, 583–589 (2023).
22. Coyne, M. J. *et al.* Phylum-wide general protein O-glycosylation system of the Bacteroidetes. *Mol Microbiol* **88**, 772–783 (2013).

23. Posch, G. *et al.* “Cross-glycosylation” of proteins in Bacteroidales species. *Glycobiology* **23**, 568 (2013).
24. Lauber, F., Cornelis, G. R. & Renzi, F. Identification of a new lipoprotein export signal in gram-negative bacteria. *mBio* **7**, 1232–1248 (2016).
25. Josts, I., Veith, K., Normant, V., Schalk, I. J. & Tidow, H. Structural insights into a novel family of integral membrane siderophore reductases. *Proc Natl Acad Sci U S A* **118**, e2101952118 (2021).
26. Rocha, E. R. & Krykunivsky, A. S. Anaerobic utilization of Fe(III)-xenosiderophores among Bacteroides species and the distinct assimilation of Fe(III)-ferrichrome by Bacteroides fragilis within the genus. *Microbiologyopen* **6**, e00479 (2017).
27. Jumper, J. *et al.* Highly accurate protein structure prediction with AlphaFold. *Nature 2021 596:7873* **596**, 583–589 (2021).
28. Pollet, R. M., Martin, L. M. & Koropatkin, N. M. TonB-dependent transporters in the Bacteroidetes: Unique domain structures and potential functions. *Molecular Microbiology* vol. 115 490–501 Preprint at https://doi.org/10.1111/mmi.14683 (2021).
29. Madej, M. *et al.* Structural and functional insights into oligopeptide acquisition by the RagAB transporter from Porphyromonas gingivalis. *Nature Microbiology 2020 5:8* **5**, 1016–1025 (2020).
30. Glenwright, A. J. *et al.* Structural basis for nutrient acquisition by dominant members of the human gut microbiota. *Nature* **541**, 407–411 (2017).
31. Gray, D. A. *et al.* Insights into SusCD-mediated glycan import by a prominent gut symbiont. *Nat Commun* **12**, 1–14 (2021).
32. Winter, G. Xia2: An expert system for macromolecular crystallography data reduction. *J Appl Crystallogr* **43**, 186–190 (2010).
33. Evans, P. R. & Murshudov, G. N. How good are my data and what is the resolution? *Acta Crystallogr D Biol Crystallogr* **69**, 1204–1214 (2013).
34. Evans, P. Scaling and assessment of data quality. in *Acta Crystallographica Section D: Biological Crystallography* vol. 62 72–82 (International Union of Crystallography, 2006).
35. Emsley, P., Lohkamp, B., Scott, W. G. & Cowtan, K. Features and development of Coot. *Acta Crystallogr D Biol Crystallogr* **66**, 486–501 (2010).
36. Liebschner, D. *et al.* Macromolecular structure determination using X-rays, neutrons and electrons: recent developments in Phenix. *Acta Crystallogr D Struct Biol* **75**, 861–877 (2019).
37. Chen, V. B. *et al.* MolProbity: all-atom structure validation for macromolecular crystallography. *Acta Crystallogr D Biol Crystallogr* **66**, 12–21 (2010).
38. Koropatkin, N. M., Martens, E. C., Gordon, J. I. & Smith, T. J. Starch Catabolism by a Prominent Human Gut Symbiont Is Directed by the Recognition of Amylose Helices. *Structure* **16**, 1105–1115 (2008).
39. Punjani, A., Zhang, H. & Fleet, D. J. Non-uniform refinement: adaptive regularization improves single-particle cryo-EM reconstruction. *Nature Methods 2020 17:12* **17**, 1214–1221 (2020).

40. Jamali, K. *et al*. Automated model building and protein identification in cryo-EM maps. *Nature 2024 628:8007* **628**, 450–457 (2024).
41. Croll, T. I. ISOLDE: A physically realistic environment for model building into low-resolution electron-density maps. *Acta Crystallogr D Struct Biol* **74**, 519–530 (2018).
42. Pettersen, E. F. *et al*. UCSF ChimeraX: Structure visualization for researchers, educators, and developers. *Protein Science* **30**, 70–82 (2021).